# Spectral Super-Resolution Neural Operator with Atmospheric Radiative Transfer Prior

Ziye Zhang<sup>®</sup>, Bin Pan<sup>®</sup>, Member, IEEE, Zhenwei Shi<sup>®</sup>, Member, IEEE

Abstract-Spectral super-resolution (SSR) aims to reconstruct hyperspectral images (HSIs) from multispectral observations, with broad applications in remote sensing. Data-driven methods are widely used, but they often overlook physical principles, leading to unrealistic spectra, particularly in atmosphere-affected bands. To address this challenge, we propose the Spectral Super-Resolution Neural Operator (SSRNO), which incorporates atmospheric radiative transfer (ART) prior into the data-driven procedure, yielding more physically consistent predictions. The proposed SSRNO framework consists of three stages: upsampling, reconstruction, and refinement. In the upsampling stage, we leverage prior information to expand the input multispectral image, producing a physically plausible hyperspectral estimate. Subsequently, we utilize a neural operator in the reconstruction stage to learn a continuous mapping across the spectral domain. Finally, the refinement stage imposes a hard constraint on the output HSI to eliminate color distortion. The upsampling and refinement stages are implemented via the proposed guidance matrix projection (GMP) method, and the reconstruction neural operator adopts U-shaped spectral-aware convolution (SAC) layers to capture multi-scale features. Moreover, we theoretically demonstrate the optimality of the GMP method. With the neural operator and ART priors, SSRNO also achieves continuous spectral reconstruction and zero-shot extrapolation. Various experiments validate the effectiveness and generalization ability of the proposed approach.

Index Terms—Spectral super-resolution, neural operator, atmospheric radiative transfer

#### I. INTRODUCTION

PECTRAL super-resolution (SSR) aims to recover hyperspectral images (HSIs) from the given RGB or multispectral image (MSI). SSR alleviates hardware limitations that prevent direct acquisition of HSIs with both high spatial and spectral resolution, thereby facilitating various downstream applications such as classification [1], [2], unmixing [3], segmentation [4], and detection [5], [6]. Nevertheless, this task is inherently ill-posed, as it requires inferring dense spectral signatures from limited and spectrally coarse observations.

Traditional SSR approaches mainly include early modelbased methods [7], regression-based methods [8], [9], and sparse representation methods [10], [11]. In remote sensing,

The work was supported by the National Key Research and Development Program of China under Grant 2022YFA1003800, the National Natural Science Foundation of China under the Grant 62571273, and the Fundamental Research Funds for the Central Universities under grant 63243074. (Corresponding author: Bin Pan.)

Ziye Zhang and Bin Pan are with the School of Statistics and Data Science, KLMDASR, LEBPS, and LPMC, Nankai University, Tianjin 300071, China (e-mail: ziyezhang@mail.nankai.edu.cn; panbin@nankai.edu.cn).

Zhenwei Shi is with the Image Processing Center, School of Astronautics, Beihang University, Beijing 100191, China (e-mail: shizhenwei@buaa.edu.cn).

they have been applied in conjunction with domain-specific priors, such as spectral unmixing features [12]. Traditional methods primarily rely on prior knowledge and physical constraints, which contribute to robustness and interpretability. However, they often fail to fully leverage large-scale data, which may lead to underfitting.

Advances in deep learning have led to a range of approaches based on deep neural networks. Numerous methods employing convolutional neural networks (CNNs) [13], [14] and attention mechanisms [15]-[17] lead to notable improvements and outperform traditional approaches. For remote sensing applications, deep learning-based methods are also widely adopted. For example, fusion-based methods [18], [19] use paired low-resolution HSIs and high-resolution MSIs to extract and fuse spectral-spatial information, producing high-resolution hyperspectral images. However, the practical application of fusion-based methods is hindered by the difficulty of obtaining registered HSI-MSI pairs. Thus, single-image spectral superresolution methods [17], [20]-[23] have gained attention, as they require only the input MSI or RGB image at the inference stage. For example, Zhou et al. [23] proposed a CNN-Transformer hybrid network for directly reconstructing hyperspectral images from RGB inputs, thereby enhancing spectral super-resolution. Unsupervised spectral super-resolution has also been extensively studied to address the challenge of acquiring paired MSI-HSI data [24]–[26]. Additionally, several studies aim to recover hyperspectral spectra at arbitrary scale [16], [27], [28], drawing inspiration from the success of implicit neural representations [29], which have been widely used in spatial super-resolution.

Data-driven methods achieve strong performance, but they often overlook underlying physical principles, resulting in unrealistic predictions. To address this, some works have sought to embed physics or priors into the data-driven framework to achieve both physical interpretability and high performance [26], [30]–[35]. For example, Lin et al. [30] incorporated spectral response functions into CNN-based models to achieve physically plausible spectral recovery. Wu et al. [35] embedded comprehensive priors to regularize and optimize the solution space of SSR. Huo et al. [34] integrated the physical relationship between spectral reflectance and corresponding RGB images via a meta-auxiliary learning strategy.

While physics-informed methods improve the plausibility of spectral reconstruction, many neglect key remote sensing factors such as solar irradiance and atmospheric transmittance, resulting in discrepancies with actual image formation. In addition, many methods are limited to a fixed number of spectral bands, restricting their applicability for arbitrary or

high-resolution spectral outputs.

To address these challenges, we propose the Spectral Super-Resolution Neural Operator (SSRNO), which embeds extraterrestrial irradiance and direct beam radiation predicted by atmospheric radiative transfer (ART) codes into a data-driven framework. Inspired by the two-stage paradigm [13], the proposed framework comprises two standard stages, upsampling and reconstruction, and an additional refinement stage, as illustrated in Figure 2. In the upsampling stage, the spectral response function (SRF) and ART priors are leveraged to generate an image with higher spectral resolution. With the upsampled HSI, we employ a data-driven neural operator to reconstruct a finer HSI estimate. Since the neural operator is resolution-invariant and coordinate-based [36], [37], we can compute the estimated HSI at arbitrary spectral scales. Finally, we refine the HSI by projecting it onto the affine space defined by the SRF, thereby ensuring consistency with the original MSI after degradation. The upsampling and refinement stages employ our proposed guidance matrix projection (GMP), a novel methodology derived from an affine space projection problem. It not only leverages physical priors to upsample the MSI but also enforces hard constraints to guarantee reconstruction consistency. Additionally, we employ a reconstruction neural operator with spectral-aware convolution (SAC) layers in a U-shaped structure to capture multi-scale spatial and spectral features. With the ART prior and the neural operator, SSRNO achieves superior continuous and zero-shot reconstruction capabilities.

The main contributions of this article are summarized below:

- We propose a physics-informed approach for spectral super-resolution, which integrates ART priors into the data-driven framework to produce physically plausible predictions;
- We derive a novel and versatile method from an affine projection formulation, enabling both upsampling and constraint incorporation, with theoretical guarantees of optimality;
- We apply the neural operator architecture to spectral reconstruction, providing physically grounded interpretability and supporting continuous spectral reconstruction.

## II. PRELIMINARIES

In this section, we introduce the preliminary works upon which our approach is built. We first introduce the atmospheric radiative transfer model in Section II-A, which forms the foundation of the physical prior used in our method. We then present the operator learning framework in Section II-B, which motivates the design of our network architecture.

#### A. Atmospheric Radiative Transfer Model

Solar radiation and atmospheric transmission modeling are crucial components of many scientific disciplines. Over the past several decades, atmospheric radiative transfer models have undergone significant evolution to meet the demands of applications ranging from climate modeling to agriculture and remote sensing. Generally, these models aim to

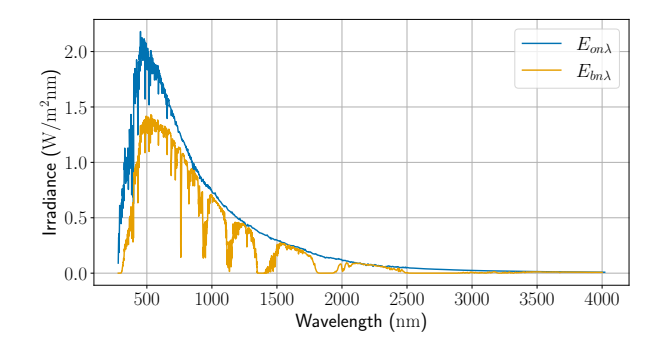


Fig. 1. Comparison to the extraterrestrial irradiance  $E_{on\lambda}$  and the direct beam radiation  $E_{bn\lambda}$ , where  $E_{on\lambda}$  is based on the Air Mass 1.5 spectra and  $E_{bn\lambda}$  is based on the 1976 U.S. Standard Atmosphere.

maintain highly accurate irradiance predictions under specific circumstances, such as vertical atmospheric profiles, seasonal variations, and geographical latitude. Examples of such models include MODerate resolution atmospheric TRANsmission (MODTRAN) [38] and Santa Barbara Disort Atmospheric Radiative Transfer (SBDART) [39]. Moreover, the Simple Model of the Atmospheric Radiative Transfer of Sunshine (SMARTS) [40] is developed to overcome the limitations of its predecessor by offering significantly improved spectral resolution, expanded atmospheric constituent modeling, and bridging the gap between high-accuracy scientific models and computational efficiency needed for solar engineering [41]. Estimating a wide spectral range from 280 nm to 4000 nm, the SMARTS includes parameterizations of gas absorption, aerosol scattering, and spectral albedo, and has been instrumental in generating standard solar spectra for photovoltaic (PV) system testing. In this article, the ART prior is from the SMARTS.

In SMARTS, the beam irradiance received at ground level by a surface oriented perpendicular to the sun rays at wavelength  $\lambda$  is defined as

$$E_{bn\lambda} = E_{on\lambda} T_{R\lambda} T_{o\lambda} T_{n\lambda} T_{q\lambda} T_{w\lambda} T_{a\lambda}, \tag{1}$$

where  $E_{bn\lambda}$  is the direct beam radiation,  $E_{on\lambda}$  is the extrater-restrial irradiance, and the transmittance factors  $T_{*\lambda}$  represent various atmospheric effects as summarized in Table I. The transmittance factors, as detailed in [40], can be computed based on the given geophysical conditions. As shown in Figure 1, the direct beam radiation exhibits several distinct absorption bands compared to the reference extraterrestrial irradiance, primarily in the range of 750-2000 nm. These features are mainly attributed to strong absorption by water vapor (H<sub>2</sub>O), carbon dioxide (CO<sub>2</sub>), and oxygen (O<sub>2</sub>). Besides, the spectral irradiance below 400 nm is also significantly absorbed by ozone (O<sub>3</sub>). In the spectral reconstruction of remote sensing imagery, the atmosphere has a substantial impact on specific wavelength bands, making it a physical factor that cannot be overlooked.

#### B. Operator Learning

Operator learning is an emerging framework in machine learning that extends the learning task from finite-dimensional

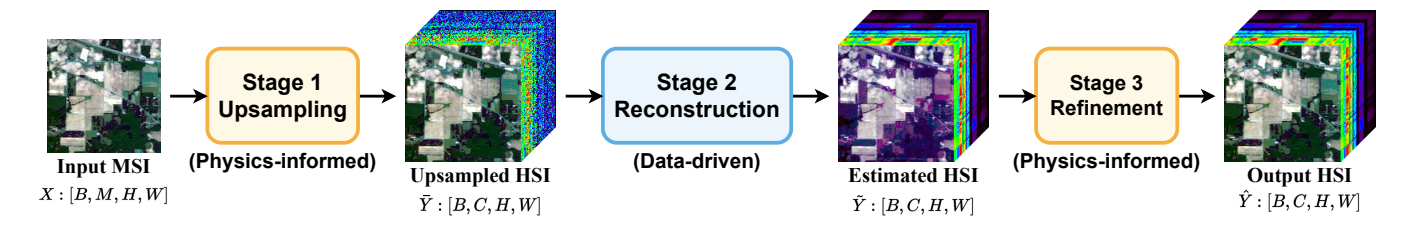


Fig. 2. Overall framework of the proposed method. The input MSI undergoes three main stages to output the final HSI  $\hat{Y}$ : (1) **Upsampling**, where we interpolate and extrapolate the input MSI to the upsampled HSI, (2) **Reconstruction**, where we employ the neural operator to transform the upsampled HSI to a finer HSI estimate, and (3) **Refinement**, where we impose a hard constraint on the final result to enforce zero reconstruction error and eliminate color distortion.

TABLE I
Atmospheric Transmittance Factors of SMARTS

Factors	Extinction process
$T_{R\lambda}$	Rayleigh scattering
$T_{o\lambda}$	Ozone (O <sub>3</sub> ) absorption
$T_{n\lambda}$	Nitrogen dioxide (NO <sub>2</sub> ) absorption
$T_{g\lambda}$	Uniformly mixed gas (mainly O2, CO2) absorption
$T_{w\lambda}$	Water vapor (H <sub>2</sub> O) absorption
$T_{a\lambda}$	Aerosol extinction

vector mappings to mappings between infinite-dimensional function spaces. Lu et al. [42] first established the deep operator network architecture, which is capable of learning continuous mappings and supporting queries at arbitrary scales.

Recently, a new model termed the *neural operator* has been proposed, which involves using neural networks to approximate mesh-free, infinite-dimensional, and nonlinear operators [36], [37], [43]. Let  $a:D\to\mathbb{R}^{d_a}$  denote the input function defined on a bounded domain  $D\subset\mathbb{R}^d$ ,  $u:D'\to\mathbb{R}^{d_a}$  denote the output function defined on  $D'\subset\mathbb{R}^d$ . Neural operators  $\mathcal{G}_\theta$  learn the non-linear mapping  $\mathcal{G}^\dagger$  between two infinite-dimensional spaces by using a finite collection of observations of input-output pairs from this mapping, which is,

$$\mathcal{G}_{\theta}: \mathcal{A} \to \mathcal{U}, \quad \theta \in \Theta,$$
 (2)

where  $\Theta$  is the parameter space,  $\mathcal{A}=\mathcal{A}(D,\mathbb{R}^{d_a})$  and  $\mathcal{U}=\mathcal{U}(D,\mathbb{R}^{d_u})$  are separable Banach spaces of function taking values in  $\mathbb{R}^{d_a}$  and  $\mathbb{R}^{d_u}$  respectively. Normally, neural operators consist of three components:

- 1) **Lifting:** Lift the input function  $\{a: D \to \mathbb{R}^{d_a}\}$  to the first hidden representation  $\{v_0: D \to \mathbb{R}^{d_{v_0}}\}$  via a pointwise function  $\mathbb{R}^{d_a} \to \mathbb{R}^{d_{v_0}}$ ;
- 2) **Iterative Kernel Integration:** Iteratively update the hidden representation

$$v_{t+1} = \sigma (W_t v_t + \mathcal{K}(a; \phi) v_t), \text{ for } t = 0, 1, ..., T - 1,$$
(3)

where  $\mathcal{K}$  is the kernel integral operator parameterized by  $\phi$ ,  $W_t: \mathbb{R}^{d_{v_t}} \to \mathbb{R}^{d_{v_{t+1}}}$  represents the linear transformation, and  $\sigma: \mathbb{R} \to \mathbb{R}$  is the activation function;

3) **Projection:** Map the last hidden representation  $\{v_T : D \to \mathbb{R}^{d_{v_T}}\}$  to the output function  $\{u : D \to \mathbb{R}^{d_u}\}$  via a point-wise function  $\mathbb{R}^{d_{v_T}} \to \mathbb{R}^{d_u}$ .

Neural operators have a wide range of mathematical and scientific applications. Beyond their utility in scientific computing, neural operators have also been applied to superresolution tasks in computer vision and remote sensing [44]–[46]. Their inherent resolution-invariance property enables continuous super-resolution, making them particularly well-suited for these applications.

#### III. METHODOLOGY

In this section, we present the SSRNO methodology. We begin by formulating the spectral reconstruction problem and outlining the motivation and overall framework of our approach in Section III-A. We then introduce two key components of the framework: the proposed guidance matrix projection method and the U-shaped reconstruction neural operator with spectral-aware kernel integrals. Section III-B discusses the GMP method and its theoretical optimality, while Section III-C provides a detailed description of the neural operator architecture.

## A. Motivation and Overall Framework

Let  $Y \in \mathbb{R}^{C \times N}$  denote the HSI,  $X \in \mathbb{R}^{M \times N}$  the paired RGB or multispectral image, and  $S \in \mathbb{R}^{M \times C}$  the SRF, where N = HW is the number of pixels, and C and M are the number of channels with C > M. Generally, SRFs contain enough information for each spectral band, so we assume that all SRF matrices are of full row rank. The relation between X and Y can be mathematically formulated in a linear matrix equation, that is,

$$SY = X. (4)$$

Thus, the spectral reconstruction problem can be formally formulated as solving the underdetermined linear matrix equation (4), where, given an RGB or multispectral image X and its corresponding spectral response function S, the objective is to recover a plausible solution  $\hat{Y}$  to (4).

To solve this ill-posed problem, a widely used approach is the two-stage reconstruction paradigm, where the input is first upsampled to the target resolution or modality space, followed by a data-driven reconstruction module that restores missing details and corrects estimation errors [13]. This paradigm can be formulated as

$$\hat{Y} = R(U(X)) + U(X),\tag{5}$$

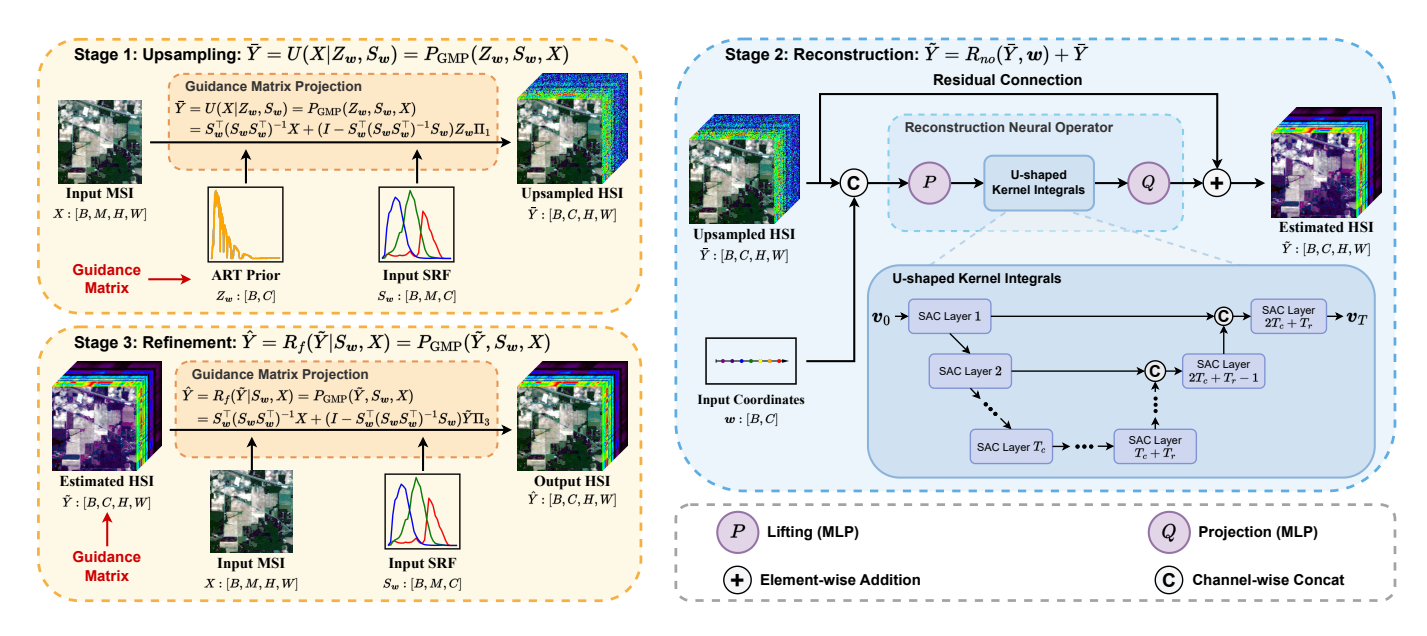


Fig. 3. Overview of the upsampling, reconstruction, and refinement stages. The upsampling and refinement stages both employ the GMP method, but with different objectives. In the upsampling stage, GMP incorporates prior knowledge to produce a physically plausible HSI estimate, whereas in the refinement stage, it projects the HSI onto the affine space defined by (4). The reconstruction stage employs a neural operator with a U-shaped structure and spectral-aware convolution layers to learn the mapping from upsampled HSIs to target HSIs across continuous spectral dimensions.

where  $U(\cdot)$  denotes the upsampling operation that projects the input X into a higher-dimensional target space, and  $R(\cdot)$  is a learnable data-driven reconstruction module, such as CNN-based neural networks. A residual connection is employed to facilitate learning and enhance reconstruction quality.

However, this paradigm faces inherent limitations when applied to spectral reconstruction. For the upsampler  $U(\cdot)$ , commonly used techniques such as bilinear interpolation and transposed convolution are less effective in spectral superresolution, as the upsampling ratio is substantially higher than in typical spatial super-resolution tasks. Additionally, this paradigm is entirely data-driven, lacking integration of physical processes such as atmospheric transmission and sensor response that are essential for spectral reconstruction. Besides, most data-driven reconstruction modules rely on deep neural networks that learn mappings between finite-dimensional spaces. However, such designs neglect the continuity of spectral signatures, thereby limiting both performance and applicability.

Hence, inspired by (5) and prior studies on multistage frameworks [47], we adopt a similar yet more effective three-stage design, as illustrated in Figure 2. Given the MSI X, wavelength coordinates w, and the SRF  $S_w$  discretized at w, we sequentially apply the following three stages to obtain the final HSI estimate.

1) **Upsampling:** In the first upsampling stage, we apply the proposed GMP method to obtain the initial upsampled HSI, which can be formulated as

$$\bar{Y} = U(X|Z_{\boldsymbol{w}}, S_{\boldsymbol{w}}) = P_{\text{GMP}}(Z_{\boldsymbol{w}}, S_{\boldsymbol{w}}, X), \tag{6}$$

where  $U(\cdot|Z_{\boldsymbol{w}},S_{\boldsymbol{w}})$  is the conditional upsampler guided by  $Z_{\boldsymbol{w}}$  and  $S_{\boldsymbol{w}}$ ,  $P_{\text{GMP}}(\cdot,\cdot,\cdot)$  is our proposed guidance matrix projector with given pixel-wise prior  $Z_{\boldsymbol{w}} \in \mathbb{R}^{C \times N}$ 

as the guidance matrix, SRF  $S_{\pmb{w}} \in \mathbb{R}^{M \times C}$  and MSI  $X \in \mathbb{R}^{M \times N}$ , which are all discretized at  $\pmb{w}$ .

2) Reconstruction: In the next reconstruction stage, we employ a resolution-invariant neural operator with a Ushaped structure to learn the mapping between infinitedimensional spaces of upsampled and target HSIs, which can be formulated as

$$\tilde{Y} = R_{no}(\bar{Y}, \boldsymbol{w}) + \bar{Y},\tag{7}$$

where  $\tilde{Y}$  is the reconstructed HSI,  $R_{no}(\cdot, \cdot)$  is the neural operator that takes the functional value and the coordinate as inputs, and a residual connection is employed similar to Equation (5).

3) **Refinement:** In the final refinement stage, we project our final output to the solution space of (4), which imposes a hard constraint on our result. This stage can be formulated as

$$\hat{Y} = R_f(\tilde{Y}|S_{\boldsymbol{w}}, X) = P_{\text{GMP}}(\tilde{Y}, S_{\boldsymbol{w}}, X), \tag{8}$$

where  $\hat{Y}$  is the output HSI,  $R_f(\cdot|S_{\boldsymbol{w}},X)$  is the refinement operator. Although the  $R_f(\cdot|S_{\boldsymbol{w}},X)$  employs the same GMP procedure as the upsampler in the first stage, its objective is fundamentally different. The upsampling stage aims to produce a physically plausible upsampled HSI. In contrast, the refinement stage projects our final output to the solution space of (4), which imposes a hard constraint on our result.

Our framework successfully addresses the limitations of the traditional two-stage paradigm. First, the GMP method embeds physical priors into the data-driven framework through pixel-wise guidance. It also refines the output by solving a constrained optimization problem, thereby enforcing the hard constraint defined in (4). Moreover, previous studies have shown that neural operators can accommodate inputs defined on meshes with different discretizations [36], [37], so we employ a neural operator to address the inherent limitation of conventional neural networks that can only model discrete spectral vectors.

Within the proposed framework, the guidance matrix projection method and the reconstruction neural operator serve as two core components, which are detailed in Section III-B and Section III-C, respectively.

## B. Guidance Matrix Projection

In this section, we propose a novel method termed Guidance Matrix Projection, based on the formulation in Section III-A. We seek a physically plausible HSI estimate that remains close to the guidance matrix Z while satisfying the constraint in (4). To achieve this, we can consider the following affine space projection problem:

$$\min_{Y} \quad SAM(Y, Z)$$
s.t.  $SY = X$ , (9)

where  $SAM(\cdot, \cdot)$  denotes the Spectral Angle Mapper (SAM), a widely used metric for measuring spectral similarity between two HSIs. It is defined as

$$SAM(Y, Z) = \frac{1}{N} \sum_{n} \arccos\left(\frac{Y_{\cdot n}^{\top} Z_{\cdot n}}{\|Y_{\cdot n}\| \|Z_{\cdot n}\|}\right), \quad (10)$$

where  $\|\cdot\|$  is the L2 norm,  $Y_{\cdot n}$  denote the nth column vector of Y, that is, the discretized spectral curve of Y at pixel n. Equivalently, it suffices to solve

$$\max \frac{Y_{.n}^{\top} Z_{.n}}{\|Y_{.n}\| \|Z_{.n}\|}$$
s.t.  $SY_{.n} = X_{.n}$ . (11)

for n = 1, 2, ..., N. Therefore, our goal is to find an appropriate spectral estimate  $Y_{\cdot n}$  within the affine space  $\mathcal{A}_n(S, X_{\cdot n}) =$  $\{ \boldsymbol{v} \in \mathbb{R}^C : S\boldsymbol{v} = X_{\cdot n} \}$  that minimizes the spectral angle (or equivalently maximizes the cosine similarity) with the prior  $Z_{n}$ , for each pixel  $n = 1, 2, \dots, N$ .

However, the non-trivial solution to problem (11) may not exist. To address this, we impose the following assumption.

**Assumption 1.** For all n = 1, 2, ..., N, the SRF matrix  $S \in$  $\mathbb{R}^{M \times C}$ , prior  $Z_{\cdot n} \in \mathbb{R}^C$ , and MSI pixel value  $X_{\cdot n} \in \mathbb{R}^M$ 

(1) 
$$\alpha_n \triangleq X_{.n}^{\top}(SS^{\top})^{-1}SZ_{.n} > 0;$$
  
(2)  $\beta_n \triangleq Z_{.n}^{\top}(I - S^{\top}(SS^{\top})^{-1}S)Z_{.n} > 0;$   
(3)  $\gamma_n \triangleq X_{.n}^{\top}(SS^{\top})^{-1}X_{.n} > 0.$ 

(2) 
$$\beta_n \triangleq Z_{\cdot n}^{\top} (I - S^{\top} (SS^{\top})^{-1} S) Z_{\cdot n} > 0$$

(3) 
$$\gamma_n \triangleq X_n^{\top} (SS^{\top})^{-1} X_{n} > 0$$

Recall that in Section III-A we assume S has full row rank, ensuring that  $(SS^{\top})^{-1}$  exists. Built on the assumption and inspired by recent works on range-nullspace decomposition [48], [49], we establish the following theorem, which provides the solution to (11).

**Theorem 1.** Under Assumption 1, the problem (11) for each n = 1, 2, ..., N has non-trivial solution

$$Y_{\cdot n}^* = S^{\top} (SS^{\top})^{-1} X_{\cdot n} + \left( I - S^{\top} (SS^{\top})^{-1} S \right) \frac{\gamma_n}{\alpha_n} Z_{\cdot n}. \tag{12}$$

*Proof.* Let  $S^{\dagger} = S^{\top}(SS^{\top})^{-1}$  denote the Moore-Penrose inverse of S. To facilitate the derivation, we first decompose  $Y_{\cdot n}$  and  $Z_{\cdot n}$  into components lying in the range space  $\mathcal{R}(S^\dagger) = \{S^\top (SS^\top)^{-1} \boldsymbol{u} : \boldsymbol{u} \in \mathbb{R}^M\}$  and the null space  $\mathcal{N}(S) = \{ v \in \mathbb{R}^C : Sv = 0 \}$ , i.e., the range-null space decomposition:

$$Y_{\cdot n} = S^{\top} (SS^{\top})^{-1} X_{\cdot n} + \left( I - S^{\top} (SS^{\top})^{-1} S \right) Y_{\cdot n}$$
  

$$\triangleq Y_{n \mathcal{R}} + Y_{n \mathcal{N}}, \tag{13}$$

$$Z_{\cdot n} = S^{\top} (SS^{\top})^{-1} S Z_{\cdot n} + \left( I - S^{\top} (SS^{\top})^{-1} S \right) Z_{\cdot n}$$
  

$$\triangleq Z_{\cdot n, \mathcal{R}} + Z_{\cdot n, \mathcal{N}}. \tag{14}$$

In this decomposition,  $Y_{n,\mathcal{N}}$  is the only optimization variable, whereas  $Z_{\cdot n,\mathcal{R}}$ ,  $Z_{\cdot n,\mathcal{N}}$ , and  $Y_{\cdot n,\mathcal{R}}$  are fixed and known. By the orthogonality between the range space  $\mathcal{R}(S^{\dagger})$  and the null space  $\mathcal{N}(S)$ , the objective function of problem (11) can be expressed as

$$\frac{Y_{\cdot n}^{\top} Z_{\cdot n}}{\|Y_{\cdot n}\| \|Z_{\cdot n}\|} = \frac{1}{\|Z_{\cdot n}\|} \frac{(Y_{\cdot n, \mathcal{R}} + Y_{\cdot n, \mathcal{N}})^{\top} (Z_{\cdot n, \mathcal{R}} + Z_{\cdot n, \mathcal{N}})}{\|Y_{\cdot n, \mathcal{R}} + Y_{\cdot n, \mathcal{N}}\|} 
= \frac{1}{\|Z_{\cdot n}\|} \frac{Y_{\cdot n, \mathcal{R}}^{\top} Z_{\cdot n, \mathcal{R}} + Y_{\cdot n, \mathcal{N}}^{\top} Z_{\cdot n, \mathcal{N}}}{\sqrt{\|Y_{\cdot n, \mathcal{R}}\|^2 + \|Y_{\cdot n, \mathcal{N}}\|^2}}.$$
(15)

Therefore, problem (11) can be equivalently reformulated as

$$\max_{Y_{\cdot n, \mathcal{N}} \in \mathcal{N}(S)} \frac{Y_{\cdot n, \mathcal{R}}^{\top} Z_{\cdot n, \mathcal{R}} + Y_{\cdot n, \mathcal{N}}^{\top} Z_{\cdot n, \mathcal{N}}}{\sqrt{\|Y_{\cdot n, \mathcal{R}}\|^2 + \|Y_{\cdot n, \mathcal{N}}\|^2}}.$$
 (16)

The problem (16) attains its optimum if and only if  $Y_{n,\mathcal{N}}$  and  $Z_{n,\mathcal{N}}$  are collinear, so that their inner product in the numerator is maximized. Hence, let  $Y_{n,\mathcal{N}} = \xi Z_{n,\mathcal{N}}, \ \xi \geq 0$ , and the problem can be further simplified to a univariate optimization problem:

$$\max_{\xi \ge 0} \quad g(\xi), \tag{17}$$

where the objective function  $q(\xi)$  can be derived as

$$g(\xi) = \frac{Y_{\cdot n, \mathcal{R}}^{\top} Z_{\cdot n, \mathcal{R}} + \|Z_{\cdot n, \mathcal{N}}\|^{2} \xi}{\sqrt{\|Y_{\cdot n, \mathcal{R}}\|^{2} + \|Z_{\cdot n, \mathcal{N}}\|^{2} \xi^{2}}}$$
$$= \frac{\alpha_{n} + \beta_{n} \xi}{\sqrt{\gamma_{n} + \beta_{n} \xi^{2}}},$$
(18)

where  $\alpha_n$ ,  $\beta_n$ , and  $\gamma_n$  are defined in Assumption 1. We proceed by differentiating  $g(\xi)$  to find the optimal solution. The derivative of  $q(\xi)$  is

$$g'(\xi) = \frac{\beta_n \gamma_n - \alpha_n \beta_n \xi}{(\beta_n \xi^2 + \gamma_n)^{\frac{3}{2}}}.$$
 (19)

By Assumption 1, we conclude that  $g'(\xi) > 0$  for  $\xi \in$  $[0, \gamma_n/\alpha_n)$  and  $g'(\xi) < 0$  for  $\xi \in (\gamma_n/\alpha_n, +\infty)$ . Thus,  $g(\xi)$ takes maximum value at  $\xi^* = \gamma_n/\alpha_n$ , yielding the optimal solution for problem (11) as

$$Y_{\cdot n}^* = Y_{\cdot n, \mathcal{R}} + \xi^* Z_{\cdot n, \mathcal{N}}$$
  
=  $S^{\top} (SS^{\top})^{-1} X_{\cdot n} + (I - S^{\top} (SS^{\top})^{-1} S) \frac{\gamma_n}{\alpha_n} Z_{\cdot n}.$  (20)

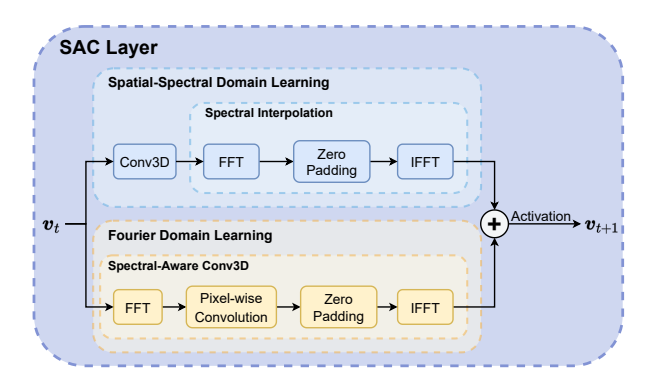


Fig. 4. Architecture of the spectral-aware convolution layer. The input  $v_t$  goes through two parallel streams: Fourier domain learning and spatial-spectral domain learning. Two outputs are added up, passed through the activation function, and result in the output  $v_{t+1}$ .

Therefore, for each pixel  $n=1,2,\ldots,N$ , the optimum upsampled spectral curve  $Y_{\cdot n}^*$  is obtained as given in (12). Finally, by concatenating all  $Y_{\cdot n}^*$ , we obtain the final result in matrix form and define the GMP operator as

$$P_{\text{GMP}}(Z, S, X) \triangleq Y^* = S^{\dagger} X + P_S Z \Pi, \tag{21}$$

where  $S^\dagger=S^\top(SS^\top)^{-1}$  is the Moore-Penrose inverse of  $S,\ P_S=I-S^\top(SS^\top)^{-1}S$  is the orthogonal projection matrix onto null space  $\mathcal{N}(S)$ , and  $\Pi$  is the diagonal matrix of coefficients  $\gamma_n/\alpha_n$  given by

$$\Pi = \begin{pmatrix} \frac{\gamma_1}{\alpha_1} & & & \\ & \frac{\gamma_2}{\alpha_2} & & \\ & & \ddots & \\ & & & \frac{\gamma_N}{\alpha_N} \end{pmatrix} .$$
(22)

Given X, S, and Z, the upsampled HSI can be computed in closed form using (21), without the need for any iterative optimization or training procedure. Additionally, Assumption 1 is generally mild and commonly satisfied in practical scenarios, thus ensuring the broad applicability of the GMP method.

#### C. Reconstruction Neural Operator

In this section, we introduce the neural operator architecture for the reconstruction stage. In this stage, we aim to learn the continuous mapping between the upsampled HSI  $\bar{Y}$  and the target HSI Y via a data-driven neural network. The output  $\tilde{Y}$  in (7) is expected to be more informative and more accurate than the input  $\bar{Y}$ , i.e., closer to the ground truth Y.

An overview of the neural operator architecture is provided in Figure 3, with its layer-wise structure shown in Figure 4. Building on advances in Fourier domain learning for image reconstruction [50] and neural operator design [43], we adopt a spectral-aware convolution module and integrate a U-shaped structure to enable multi-scale extraction of spatial and spectral features. The SAC module performs Fourier transforms across both spectral and spatial dimensions, while restricting the pixel-wise convolution to the spectral domain using a fixed set of Fourier modes. The algorithm of the spectral-aware convolution is shown in Algorithm 1.

#### Algorithm 1 Spectral-Aware Convolution

**Require:** Input tensor  $x : [B, d_{in}, H, W, C]$ , weight  $W : [d_{in}, d_{out}, d_{modes}]$ .

- 1: Transform x to Fourier domain:
- 2:  $\tilde{x} \leftarrow \text{rfft}(x)$  # shape:  $[B, d_{\text{in}}, H, W, C//2 + 1]$
- 3: Initialize output in frequency domain:
- 4:  $\tilde{y} \leftarrow 0$  # shape:  $[B, d_{\text{out}}, H, W, C//2 + 1]$
- 5: Pixel-wise convolution:
- $\tilde{y}[...,:d_{\text{modes}}] \leftarrow \text{einsum}($
- 7: "bixyz,ioz  $\rightarrow$  boxyz",
- 8:  $\tilde{x}[...,:d_{\text{modes}}], W$
- 9: )
- 10: Apply inverse Fourier transform:
- 11:  $x \leftarrow \operatorname{irfft}(\tilde{y})$
- 12: **return**  $\tilde{y}$

In general, based on the formulation of the neural operator in Section II-B, the structure of the reconstruction neural operator  $R_{no}(\cdot, \boldsymbol{w})$  can be summarized as follows.

1) **Lifting:** The upsampled HSI  $\bar{Y}$ , together with the input coordinate w, is lifted into a higher-dimensional feature space through a multilayer perceptron (MLP), formulated as

$$\tilde{Y}_0 = \text{MLP}_P\left(\text{Concat}\left(\bar{Y}, \boldsymbol{w}\right)\right),$$
 (23)

where  $\tilde{Y}_0$  is the first hidden representation,  $\operatorname{Concat}(\cdot)$  is the concatenation operation, and trivial reshaping and expanding operations are omitted for clarity.

2) **U-shaped Kernel Integration:** We iteratively update the hidden representation through several U-shaped SAC layers to yield the next representation, as illustrated in Figure 3 and Figure 4. To formulate this, let  $T_c$  be the number of layers in the contracting path and expansive path, and  $T_r$  be the number of layers in the transformation path. The iterative updates in the contracting path and transformation path can be formulated as

$$\tilde{Y}_{t+1} = \sigma \left( \mathcal{L}_t \left( \tilde{Y}_t \right) + \text{SAC}_t \left( \tilde{Y}_t \right) \right),$$
 (24)

where  $t=0,1,\ldots,T_c-1,T_c,\ldots,T_c+T_r-1$ ,  $\mathcal{L}_t(\cdot)$  and  $SAC_t(\cdot)$  represent the linear convolution operator in the spatial-spectral domain and the spectral-aware convolution operator in the Fourier domain at t step respectively, and  $\sigma(\cdot)$  is the activation function. While for the expansive path, the iterative updates can be expressed as

$$\tilde{Y}_{t+1} = \sigma \left( \mathcal{S}_t \left( \text{Concat} \left( \tilde{Y}_t, \tilde{Y}_{2T_c + T_r - 1 - t} \right) \right) \right), \quad (25)$$

where  $t = T_c + T_r, \dots, 2T_c + T_r - 1$ ,  $\mathcal{S}_t(\cdot) = \mathcal{L}_t(\cdot) + SAC_t(\cdot)$ .

3) **Projection:** We finally map the last hidden representation  $\tilde{Y}_{2T_c+T_r}$  to the estimated HSI  $\tilde{Y}$  via another MLP, that is.

$$\tilde{Y} = \text{MLP}_Q \left( \tilde{Y}_{2T_c + T_r} \right). \tag{26}$$

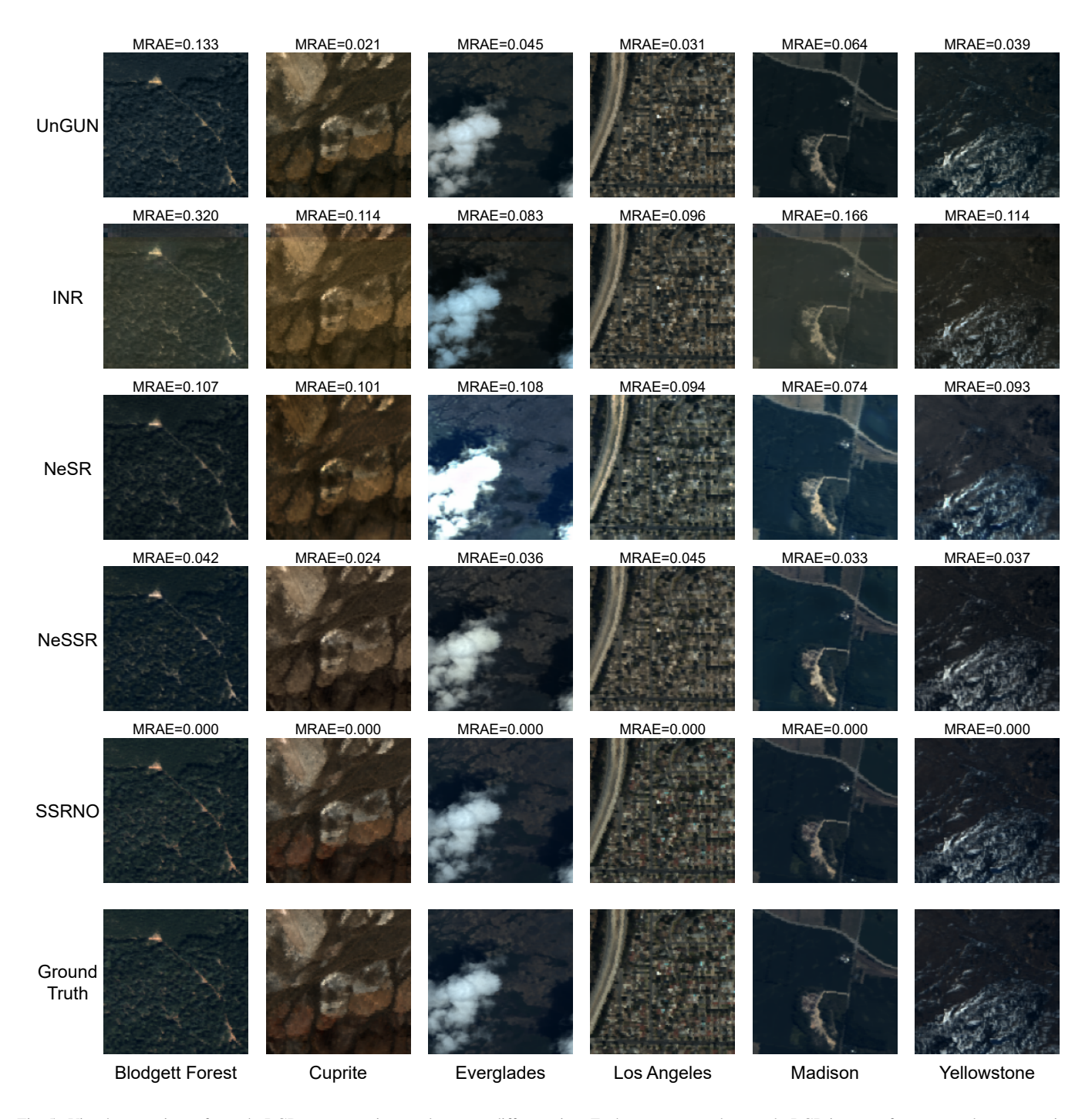


Fig. 5. Visual comparison of pseudo-RGB reconstruction results across different sites. Each row presents the pseudo-RGB images of one spectral reconstruction method applied to one scene from six different sites, while each column compares the pseudo-RGB images of various methods on the same scene within a single site. The MRAE reconstruction error is also calculated and presented on top of the image.

# IV. EXPERIMENTS

In this section, we present numerical experiment results to validate our approach under various settings. We begin by introducing the datasets in Section IV-A and outlining the basic experimental setups in Section IV-B. Comparisons with several baselines are reported in Section IV-C, followed by an ablation study in Section IV-D. Finally, experiments on arbitrary-scale and zero-shot spectral reconstruction are conducted in Section IV-E to further assess the generalization

capability of the model.

# A. Datasets

We collect data from the NASA Jet Propulsion Laboratory (JPL), originally acquired by the widely recognized AVIRIS (Airborne Visible/Infrared Imaging Spectrometer) sensors, and curate it into a new dataset for our study<sup>1</sup>. The dataset comprises hyperspectral images spanning 224 contiguous spectral

<sup>&</sup>lt;sup>1</sup>Data available at https://aviris.jpl.nasa.gov/dataportal

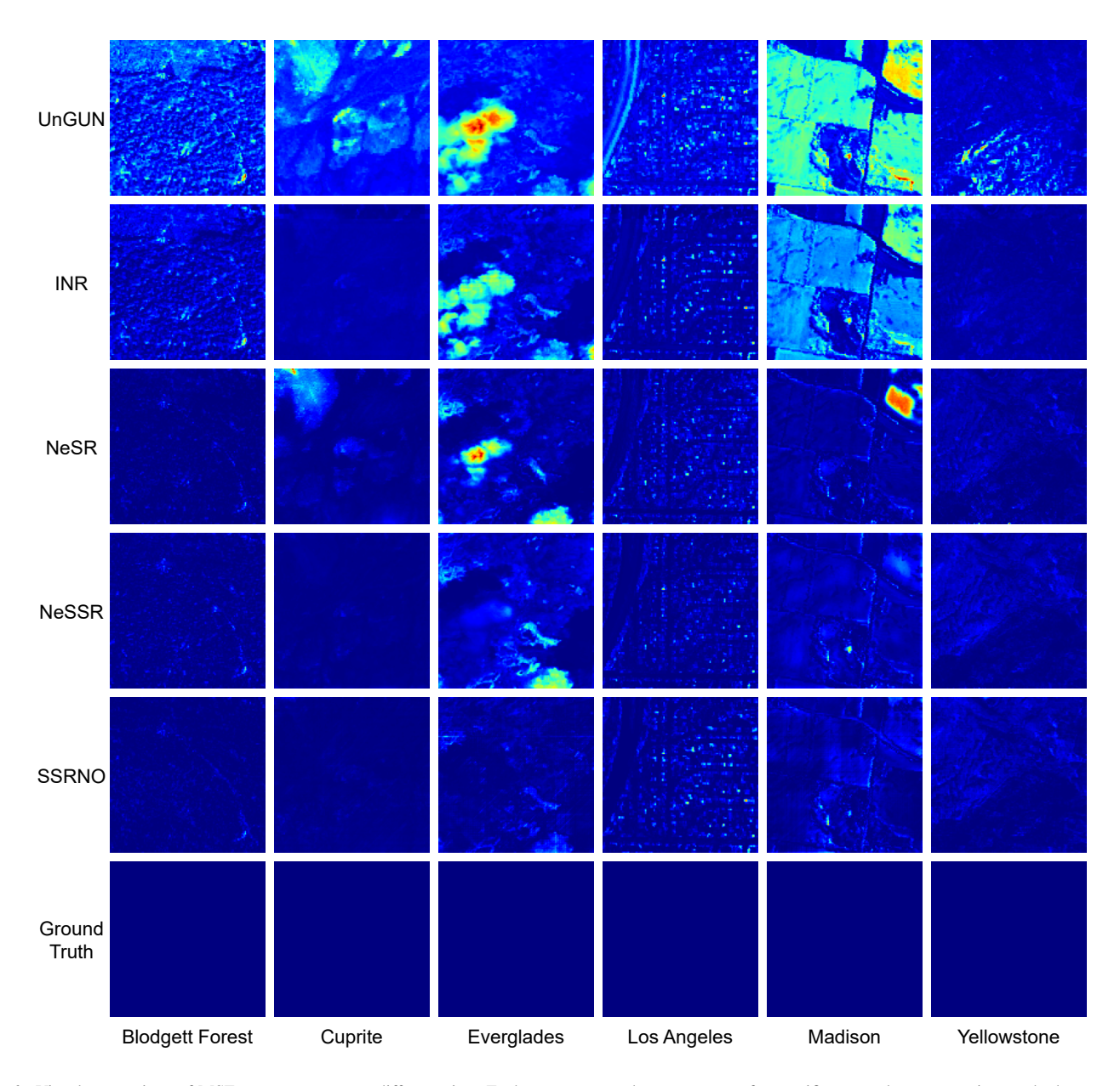


Fig. 6. Visual comparison of MSE error maps across different sites. Each row presents the error maps of a specific spectral reconstruction method on a scene from six sites, while each column shows the error maps of different methods applied to the same scene of a given site.

bands, ranging from 400 to 2500 nm. Specifically, we select various typical and representative sites, each comprising multiple scenes. The scene characteristics, such as season and spatial resolution, are consistent within each site but differ significantly across different sites. The summary of sites used in our experiment is provided in Table II.

# B. Implementation Details

1) Basic Setup: In our experiments, we use the direct beam radiation predicted by SMARTS [40] based on the 1976 U.S. Standard Atmosphere as the ART prior, which serves as the prior Z in (6). For the SRF, we utilize the database provided by [51], which includes 28 camera sensitivity functions covering a variety of types. We generate the paired RGB image by multiplying the normalized SRF randomly selected from the

TABLE II
AVIRIS SITES SELECTED FOR THE EXPERIMENTS

Site Name	Land Cover Type	Flight ID	Resolution (m)	
Blodgett Forest	Forest	f130803t01	3.6	
Cuprite	Desert	f060502t01	3.4	
Everglades	Wetland	f100523t01	17	
Los Angeles	Urban area	f130821t01	3.5	
Madison	Rural area	f110816t01	7.4	
Yellowstone	Mountainous area	f060925t01	15.1	

database and the HSI from the AVIRIS dataset we collected in Section IV-A. For hyperparameters of the neural operator, we set maximum Fourier modes  $d_{\rm modes}=16$ , number of hidden channels d=32, and number of contracting and

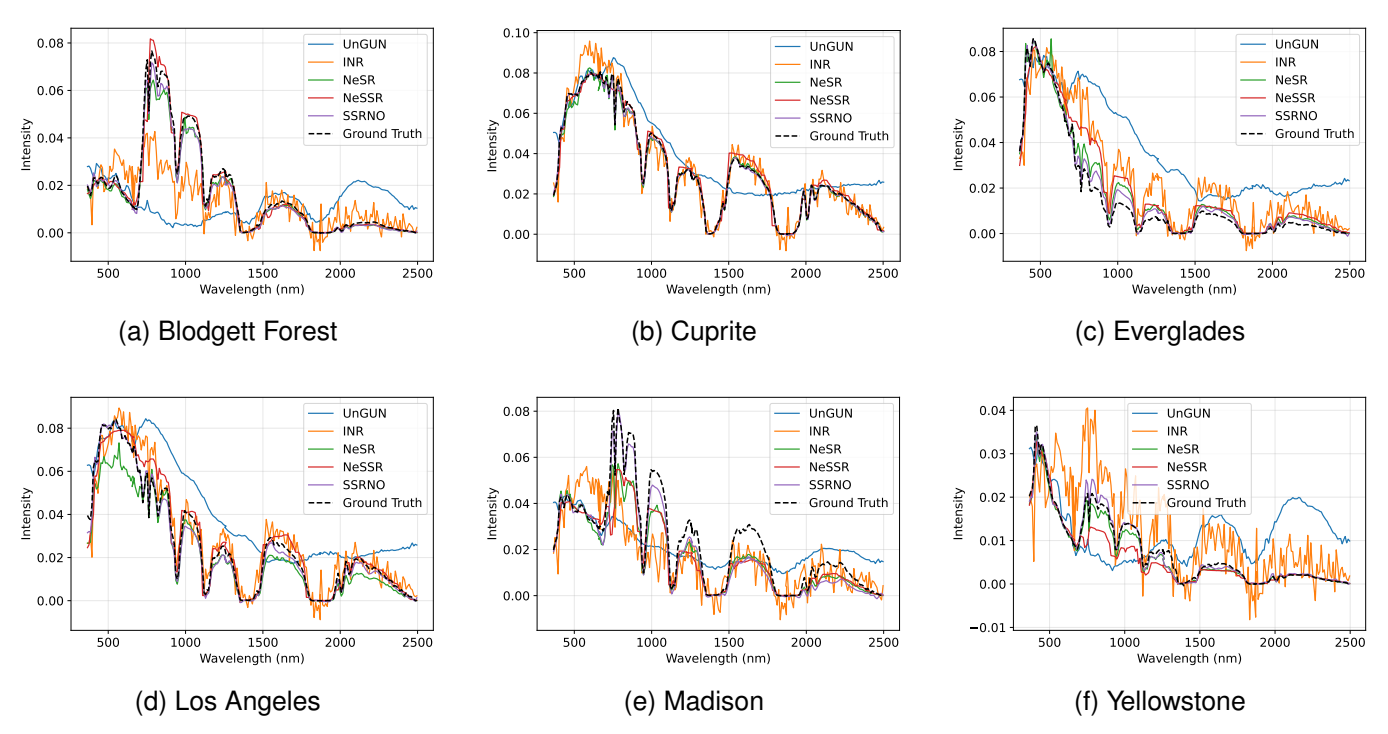


Fig. 7. Comparison of predicted spectral signatures for representative reconstructed pixels from six benchmark sites (Blodgett Forest, Cuprite, Everglades, Los Angeles, Madison, and Yellowstone), reconstructed using different methods.

transformation layers  $T_c = T_r = 4$ . Coordinate-based terms, including SRF  $S_w$  and ART prior  $Z_w$ , are interpolated at wavelength w via kernel regression.

2) Loss Function: In our experiments, we construct the loss function of our model by adding up the L1 and the SAM criterion, which is

$$\mathcal{L}(\hat{Y}, Y) = L_1(\hat{Y}, Y) + \lambda \text{SAM}(\hat{Y}, Y), \tag{27}$$

where  $\lambda$  is the trade-off parameter (we set  $\lambda=0.1$  in our experiments), SAM $(\cdot,\cdot)$  is defined in (10), and  $L_1(\cdot,\cdot)$  is calculated by

$$L_1(\hat{Y}, Y) = \frac{1}{CN} \sum_{c,n} |\hat{Y}_{cn} - Y_{cn}|.$$
 (28)

3) Metrics: We adopt four commonly used metrics to evaluate the reconstruction performance: the Mean Relative Absolute Error (MRAE), the Peak Signal-to-Noise Ratio (PSNR), the Structural Similarity Index Measure (SSIM), and the SAM. Lower MRAE and SAM values, together with higher PSNR and SSIM, indicate better reconstruction quality.

## C. Comparative Experiments

We conduct comparative experiments to evaluate the effectiveness of the proposed SSRNO against several representative methods, including UnGUN [24], INR [22], NeSR [16], and NeSSR [28]. All models are evaluated under the same training-testing protocol using the full-resolution spectral super-resolution setting.

Table III reports the overall quantitative results on the test datasets. Among all baselines, our SSRNO consistently

achieves the best performance, with the lowest MRAE and SAM, the highest PSNR and SSIM, and the fewest parameters among high-performing methods. These results highlight the efficiency and effectiveness of our design. Furthermore, we also conduct per-site evaluations on six representative scenes, and the results are summarized in Table IV. SSRNO consistently delivers top or near-top performance in most scenarios, particularly excelling in complex scenes such as rural areas. This demonstrates that the model is highly generalizable and adaptable to heterogeneous landforms and spectral distributions

We also conduct a visual comparison among all models, as shown in Figure 5, Figure 6, and Figure 7. Figure 5 demonstrates that our method is capable of faithfully restoring RGB images, whereas other methods exhibit visual artifacts or unnatural color distortions. This advantage mainly stems from the refinement step, which explicitly enforces zero reconstruction loss with GMP, ensuring accurate color consistency. The error maps in Figure 6 further highlight the superiority of our method. Additionally, we plot the predicted spectrum on six sites, which are shown in Figure 7. Our method yields more natural and physically plausible spectra that better align with the ground-truth, especially in wavelength regions affected by atmospheric absorption, whereas other approaches tend to either overfit noisy variations or underfit the true reflectance shape.

In general, both quantitative and qualitative comparisons indicate that SSRNO achieves state-of-the-art performance and more stable results across varied geographical contexts with fewer parameters.

TABLE III
COMPARATIVE RESULTS ON THE OVERALL DATASETS

Method	Params (M)	Arbitrary-scale	MRAE ↓	PSNR ↑	SAM ↓	SSIM ↑
UnGUN [24]	1.1	Х	0.611	35.167	0.536	0.808
INR [22]	63.9	×	0.366	39.592	0.312	0.906
NeSR [16]	29.3	✓	0.190	42.885	0.142	0.954
NeSSR [28]	5.3	✓	0.186	43.367	0.178	0.963
SSRNO (Ours)	4.8	✓	0.160	45.400	0.137	0.973

TABLE IV COMPARATIVE RESULTS FOR EACH SITE

	Blodgett Forest		Cuprite		Everglades		Los Angeles		Madison		Yellowstone	
Method Forest		Desert		Wetland		Urban area		Rural area		Mountainous area		
	PSNR ↑	SAM ↓	PSNR ↑	SAM ↓	PSNR ↑	SAM ↓	PSNR ↑	SAM ↓	PSNR ↑	SAM ↓	PSNR ↑	SAM ↓
UnGUN [24]	32.537	1.001	36.546	0.310	33.005	0.455	34.616	0.454	31.402	0.805	39.468	0.578
INR [22]	35.984	0.483	44.403	0.130	35.584	0.331	39.402	0.254	33.313	0.497	42.553	0.390
NeSR [16]	42.910	0.106	48.152	0.064	36.803	0.199	40.186	0.150	38.686	0.181	46.416	0.184
NeSSR [28]	41.353	0.193	48.489	0.086	39.324	0.240	42.376	0.164	38.856	0.208	44.968	0.242
SSRNO (Ours)	43.296	0.112	53.423	0.049	42.188	0.183	<u>41.884</u>	0.148	41.601	0.125	<u>45.575</u>	0.221

TABLE V
QUANTITATIVE EVALUATION OF CONTINUOUS (INTERPOLATION) AND ZERO-SHOT (EXTRAPOLATION) SPECTRAL RECONSTRUCTION

Method	Co	ntinuous (I	nterpolation	1)	Zero-shot (Extrapolation)			
	MRAE ↓	PSNR ↑	SAM ↓	SSIM ↑	MRAE ↓	PSNR ↑	SAM ↓	SSIM ↑
NeSR [16]	0.565	34.116	0.374	0.681	0.967	30.709	0.860	0.532
NeSSR [28]	0.563	34.309	0.528	0.685	1.054	30.049	0.664	0.584
SSRNO (Ours)	0.220	43.144	0.194	0.944	0.707	34.457	0.641	0.765

#### D. Ablation Study

In this section, we conduct ablation studies to further investigate the effectiveness of the proposed method. The key innovation of our method lies in the GMP, which integrates physical priors into a data-driven pipeline during the initial upsampling and enforces hard constraints during final refinement. To validate its effectiveness, we perform ablation studies on the upsampling stage and the refinement stage. For the upsampling stage, we use a zero matrix as the prior Z to obtain the upsampled HSI, rather than using the ART prior, which is also equivalent to employing the Moore-Penrose inverse. To compare the effectiveness of hard and soft constraints, we directly remove the final refinement stage and add an extra error term on the loss function as the regularization to enforce low reconstruction error, which is

$$\mathcal{L}_r(\hat{Y}, Y) = \mathcal{L}(\hat{Y}, Y) + \alpha L_1(S_{\boldsymbol{w}}\hat{Y}, S_{\boldsymbol{w}}Y), \tag{29}$$

where  $\alpha$  is the trade-off parameter, and we set  $\alpha=0.5$  in the ablation experiment. The results are listed in Table VI.

The results indicate that both the ART prior and the final refinement play critical roles in the overall performance. Removing the ART prior in the upsampling stage reduces PSNR and increases SAM, showing that physically informed guidance is crucial for producing an initial estimate close to the target. On the other hand, eliminating the refinement stage and replacing it with soft regularization degrades both PSNR and SAM significantly, suggesting that hard constraints in the output space are more effective in preserving spectral fidelity.

These findings highlight that the GMP method plays a crucial role in ensuring accurate and physically consistent spectral reconstruction.

TABLE VI ABLATION STUDY OF ART PRIOR AND REFINEMENT

ART Prior	Refinement	PSNR ↑	SAM ↓	
✓	✓	45.400	0.137	
×	✓	43.118	0.167	
✓	×	40.163	0.170	
×	×	38.760	0.178	

# E. Continuous and Zero-shot Spectral Reconstruction

To further evaluate the generalization and flexibility of our method, we conduct experiments on two challenging scenarios: continuous spectral reconstruction and zero-shot spectral reconstruction.

In the continuous reconstruction setting, we train the model using only a small number of uniformly downsampled spectral bands and test it on the full spectral resolution. This simulates an interpolation task in the spectral domain, where the model needs to infer missing spectral information between known bands. In the zero-shot setting, we train the model using only the visible spectrum range but test the model on the complete spectral range from 400 nm to 2500nm, which evaluates the ability to reconstruct the entire hyperspectral signal, including

the never-seen infrared region. This corresponds to a spectral extrapolation task, which is highly challenging due to the lack of direct observation in the infrared spectral range.

In our experiments, we apply  $2\times$  downsampling for continuous spectral reconstruction and restrict the spectrum to wavelengths below 1000 nm for zero-shot reconstruction. We compare our method against two other arbitrary-scale methods: NeSR and NeSSR. Table V summarizes the quantitative results. Our method achieves best performance in both settings, indicating strong generalization to unseen or sparsely-sampled spectral distributions.

The good performance of SSRNO stems from two factors: the neural operator backbone ensuring resolution-invariant spectral interpolation, and the ART prior guiding plausible extrapolation from visible to infrared bands. These results highlight SSRNO's robustness and generalization ability, showing that it can both interpolate missing spectra and extrapolate beyond observed bands, making it suitable for practical hyperspectral applications.

#### V. CONCLUSION

In this article, we propose a novel physics-informed approach for remote sensing image spectral reconstruction. By embedding physical priors into a data-driven framework through the GMP method, our method effectively balances interpretability and adaptability. Experiments across diverse geographical scenes indicate better reconstruction accuracy and robustness, especially in the challenging continuous and zero-shot spectral reconstruction scenarios. This work highlights the potential of integrating domain knowledge with deep learning to advance spectral super-resolution in real-world remote sensing applications.

# REFERENCES

- [1] Y. Yang, X. Tang, X. Zhang, J. Ma, F. Liu, X. Jia, and L. Jiao, "Semi-supervised multiscale dynamic graph convolution network for hyperspectral image classification," *IEEE Trans. Neural Netw. Learn.* Syst., vol. 35, no. 5, pp. 6806–6820, 2024.
- [2] X. Fu, X. Zhou, Y. Fu, P. Liu, and S. Jia, "Progressive semantic enhancement network for hyperspectral and lidar classification," *IEEE Trans. Neural Netw. Learn. Syst.*, vol. 36, no. 6, pp. 11327–11339, 2025.
- [3] Y. Su, L. Gao, A. Plaza, X. Sun, M. Jiang, and G. Yang, "SRViT: Self-supervised relation-aware vision transformer for hyperspectral unmixing," *IEEE Trans. Neural Netw. Learn. Syst.*, 2025.
- [4] H. Liu, W. Li, X.-G. Xia, M. Zhang, Z. Guo, and L. Song, "SegHSI: Semantic segmentation of hyperspectral images with limited labeled pixels," *IEEE Trans. Image Process.*, vol. 33, pp. 6469–6482, 2024.
- [5] B. Yang, Y. Mao, L. Liu, L. Fang, and X. Liu, "Change representation and extraction in stripes: Rethinking unsupervised hyperspectral image change detection with an untrained network," *IEEE Trans. Image Pro*cess., vol. 33, pp. 5098–5113, 2024.
- [6] B. Yang, C. Jiao, J. Wu, and L. Li, "Variational multiple-instance learning with embedding correlation modeling for hyperspectral target detection," *IEEE Trans. Neural Netw. Learn. Syst.*, pp. 1–15, 2024.
- [7] L. T. Maloney, "Evaluation of linear models of surface spectral reflectance with small numbers of parameters," J. Opt. Soc. Am. A, vol. 3, no. 10, pp. 1673–1683, 1986.
- [8] R. M. H. Nguyen, D. K. Prasad, and M. S. Brown, "Training-based spectral reconstruction from a single RGB image," in *Proc. Eur. Conf. Comput. Vis. (ECCV)*. Springer, 2014, pp. 186–201.
- [9] J. Wu, J. Aeschbacher, and R. Timofte, "In defense of shallow learned spectral reconstruction from RGB images," in *Proc. IEEE Int. Conf. Comput. Vis. Workshops (ICCVW)*, 2017, pp. 471–479.

- [10] B. Arad and O. Ben-Shahar, "Sparse recovery of hyperspectral signal from natural RGB images," in *Proc. Eur. Conf. Comput. Vis. (ECCV)*. Springer, 2016, pp. 19–34.
- [11] S. Zhang, H. Huang, and Y. Fu, "Fast parallel implementation of dual-camera compressive hyperspectral imaging system," *IEEE Trans. Circuits Syst. Video Technol.*, vol. 29, no. 11, pp. 3404–3414, 2018.
- [12] N. Yokoya, T. Yairi, and A. Iwasaki, "Coupled nonnegative matrix factorization unmixing for hyperspectral and multispectral data fusion," *IEEE Trans. Geosci. Remote Sens.*, vol. 50, no. 2, pp. 528–537, 2012.
- [13] Z. Shi, C. Chen, Z. Xiong, D. Liu, and F. Wu, "HSCNN+: Advanced CNN-based hyperspectral recovery from RGB images," in *Proc. IEEE Conf. Comput. Vis. Pattern Recognit. Workshops (CVPRW)*, 2018, pp. 939–947.
- [14] X. Miao, X. Yuan, Y. Pu, and V. Athitsos, "λ-Net: Reconstruct hyper-spectral images from a snapshot measurement," in *Proc. IEEE/CVF Int. Conf. Comput. Vis. (ICCV)*, 2019, pp. 4059–4069.
- [15] Y. Cai, J. Lin, Z. Lin, H. Wang, Y. Zhang, H. Pfister, R. Timofte, and L. V. Gool, "MST++: Multi-stage spectral-wise transformer for efficient spectral reconstruction," in *Proc. IEEE/CVF Conf. Comput. Vis. Pattern Recognit. (CVPR) Workshops*, June 2022, pp. 745–755.
- [16] R. Xu, M. Yao, C. Chen, L. Wang, and Z. Xiong, "Continuous spectral reconstruction from RGB images via implicit neural representation," in *Proc. Eur. Conf. Comput. Vis. (ECCV)*. Springer, 2022, pp. 78–94.
- [17] J. Li, S. Du, R. Song, Y. Li, and Q. Du, "Progressive spatial information-guided deep aggregation convolutional network for hyperspectral spectral super-resolution," *IEEE Trans. Neural Netw. Learn. Syst.*, 2023.
- [18] J. Qu, X. Wu, W. Dong, J. Cui, and Y. Li, "IR&ArF: Toward deep interpretable arbitrary resolution fusion of unregistered hyperspectral and multispectral images," *IEEE Trans. Image Process.*, vol. 34, pp. 1934– 1949, 2025.
- [19] Y. Fang, Y. Liu, C.-Y. Chi, Z. Long, and C. Zhu, "Cs2dips: Unsupervised hsi super-resolution using coupled spatial and spectral dips," *IEEE Trans. Image Process.*, vol. 33, pp. 3090–3101, 2024.
- [20] R. Dian, T. Shan, W. He, and H. Liu, "Spectral super-resolution via model-guided cross-fusion network," *IEEE Trans. Neural Netw. Learn.* Syst., vol. 35, no. 7, pp. 10059–10070, 2024.
- [21] P. Liu, Y. Zhao, K. Feng, and S. G. Kong, "Physics-driven multispectral filter array pattern optimization and hyperspectral image reconstruction," *IEEE Trans. Circuits Syst. Video Technol.*, vol. 34, no. 10, pp. 9528– 9539, 2024.
- [22] K. Zhang, D. Zhu, X. Min, and G. Zhai, "Implicit neural representation learning for hyperspectral image super-resolution," *IEEE Trans. Geosci. Remote Sens.*, vol. 61, pp. 1–12, 2023.
- [23] C. Zhou, Z. He, L. Zou, Y. Li, and A. Plaza, "HSACT: A hierarchical semantic-aware CNN-Transformer for remote sensing image spectral super-resolution," *Neurocomput.*, vol. 636, p. 129990, 2025.
- [24] Q. Qu, B. Pan, X. Xu, T. Li, and Z. Shi, "Unmixing guided unsuper-vised network for RGB spectral super-resolution," *IEEE Trans. Image Process.*, vol. 32, pp. 4856–4867, 2023.
- [25] W. Deng, J. Liu, J. Yang, Z. Wu, and L. Xiao, "Dual-path interactive U-Net for unsupervised hyperspectral image super-resolution," *IEEE J. Sel. Top. Appl. Earth Obs. Remote Sens.*, vol. 18, pp. 11751–11766, 2025.
- [26] J. Li, K. Zheng, L. Gao, Z. Han, Z. Li, and J. Chanussot, "Enhanced deep image prior for unsupervised hyperspectral image super-resolution," *IEEE Trans. Geosci. Remote Sens.*, vol. 63, pp. 1–18, 2025.
- [27] J. Li, H. Chen, W. Zhao, R. Chen, and T. Xu, "Mixed-granularity implicit representation for continuous hyperspectral compressive reconstruction," *IEEE Trans. Neural Netw. Learn. Syst.*, pp. 1–14, 2025.
- [28] R. Xu, M. Yao, C. Chen, L. Wang, and Z. Xiong, "Continuous spatial-spectral reconstruction via implicit neural representation," *Int. J. Comput. Vis.*, vol. 133, no. 1, pp. 106–128, 2025.
- [29] Y. Chen, S. Liu, and X. Wang, "Learning continuous image representation with local implicit image function," in *Proc. IEEE/CVF Conf. Comput. Vis. Pattern Recognit.*, 2021, pp. 8628–8638.
- [30] Y.-T. Lin and G. D. Finlayson, "Physically plausible spectral reconstruction from RGB images," in *Proc. IEEE/CVF Conf. Comput. Vis. Pattern Recognit. Workshops (CVPRW)*, 2020, pp. 532–533.
- [31] R. Hang, Q. Liu, and Z. Li, "Spectral super-resolution network guided by intrinsic properties of hyperspectral imagery," *IEEE Trans. Image Process.*, vol. 30, pp. 7256–7265, 2021.
- [32] J. Qu, W. Dong, Y. Li, S. Hou, and Q. Du, "An interpretable unsupervised unrolling network for hyperspectral pansharpening," *IEEE Trans. Cybern.*, vol. 53, no. 12, pp. 7943–7956, 2023.
- [33] Q. Hu, X. Wang, J. Jiang, X.-P. Zhang, and J. Ma, "Exploring the spectral prior for hyperspectral image super-resolution," *IEEE Trans. Image Process.*, vol. 33, pp. 5260–5272, 2024.

- [34] D. Huo, J. Wang, Y. Qian, and Y.-H. Yang, "Learning to recover spectral reflectance from RGB images," *IEEE Trans. Image Process.*, vol. 33, pp. 3174–3186, 2024.
- [35] C. Wu, J. Li, R. Song, Y. Li, and Q. Du, "HPRN: Holistic priorembedded relation network for spectral super-resolution," *IEEE Trans. Neural Netw. Learn. Syst.*, vol. 35, no. 8, pp. 11409–11423, 2024.
- [36] Z. Li, N. B. Kovachki, K. Azizzadenesheli, K. Bhattacharya, A. Stuart, A. Anandkumar et al., "Fourier neural operator for parametric partial differential equations," in Proc. Int. Conf. Learn. Represent. (ICLR), 2021.
- [37] N. Kovachki, Z. Li, B. Liu, K. Azizzadenesheli, K. Bhattacharya, A. Stu-art, and A. Anandkumar, "Neural operator: Learning maps between function spaces with applications to PDEs," *J. Mach. Learn. Res.*, vol. 24, no. 89, pp. 1–97, 2023.
- [38] A. Berk, G. P. Anderson, L. S. Bernstein, P. K. Acharya, H. Dothe, M. W. Matthew, S. M. Adler-Golden, J. H. C. Jr, S. C. Richtsmeier, B. Pukall et al., "MODTRAN4 radiative transfer modeling for atmospheric correction," in Proc. SPIE Opt. Spectrosc. Tech. Instrum. Atmos. Space Res. III, vol. 3756. SPIE, 1999, pp. 348–353.
- [39] P. Ricchiazzi, S. Yang, C. Gautier, and D. Sowle, "SBDART: A research and teaching software tool for plane-parallel radiative transfer in the earth's atmosphere," *Bull. Amer. Meteorol. Soc.*, vol. 79, no. 10, pp. 2101–2114, 1998.
- [40] C. Gueymard, "SMARTS2, a simple model of the atmospheric radiative transfer of sunshine: Algorithms and performance assessment," Florida Solar Energy Center, Cocoa, FL, USA, Tech. Rep. FSEC-PF-270-95, 1995.
- [41] C. A. Gueymard, "The SMARTS spectral irradiance model after 25 years: New developments and validation of reference spectra," Sol. Energy, vol. 187, pp. 233–253, 2019.
- [42] L. Lu, P. Jin, G. Pang, Z. Zhang, and G. E. Karniadakis, "Learning nonlinear operators via deeponet based on the universal approximation theorem of operators," *Nat. Mach. Intell.*, vol. 3, no. 3, pp. 218–229, 2021.
- [43] M. A. Rahman, Z. E. Ross, and K. Azizzadenesheli, "U-NO: U-shaped neural operators," *Trans. Mach. Learn. Res.*, 2023.
- [44] M. Wei and X. Zhang, "Super-resolution neural operator," in *Proc. IEEE/CVF Conf. Comput. Vis. Pattern Recognit. (CVPR)*, 2023, pp. 18 247–18 256.
- [45] Y. Zhang, H. Zheng, D. Yang, Z. Chen, H. Ma, and W. Ding, "Spacetime video super-resolution with neural operator," arXiv:2404.06036, 2024, preprint.
- [46] L. He, Z. Fang, J. Li, H. Ye, and A. Plaza, "Arbitrary-resolution hyperspectral pansharpening neural operators," *IEEE Trans. Geosci. Remote Sens.*, vol. 63, pp. 1–19, 2025.
- [47] Q. Li, Y. Yuan, X. Jia, and Q. Wang, "Dual-stage approach toward hyperspectral image super-resolution," *IEEE Trans. Image Process.*, vol. 31, pp. 7252–7263, 2022.
- [48] B. Chen, J. Song, J. Xie, and J. Zhang, "Deep physics-guided unrolling generalization for compressed sensing," *Int. J. Comput. Vis.*, vol. 131, no. 11, pp. 2864–2887, 2023.
- [49] Y. Chen, Y. Wang, and H. Zhang, "Unsupervised range-nullspace learning prior for multispectral images reconstruction," *IEEE Trans. Image Process.*, vol. 34, pp. 2513–2528, 2025.
- [50] R. Ma, Y. Zhang, B. Zhang, L. Fang, D. Huang, and L. Qi, "Learning attention in the frequency domain for flexible real photograph denoising," *IEEE Trans. Image Process.*, vol. 33, pp. 3707–3721, 2024.
- [51] J. Jiang, D. Liu, J. Gu, and S. Süsstrunk, "What is the space of spectral sensitivity functions for digital color cameras?" in 2013 IEEE Workshop on Applications of Computer Vision (WACV). IEEE, 2013, pp. 168–179.